

Suppression of turbulence and travelling waves in a vertical heated pipe

Elena Marensi^{1†}, Shuisheng He² and Ashley P. Willis¹

¹School of Mathematics and Statistics, University of Sheffield, Sheffield S3 7RH, UK

²Department of Mechanical Engineering, University of Sheffield, Sheffield S1 3JD, UK

(Received ?; revised ?; accepted ?. - To be entered by editorial office)

Turbulence in the flow of fluid through a pipe can be suppressed by buoyancy forces. As the suppression of turbulence leads to severe heat transfer deterioration, this is an important and undesirable phenomenon in both heating and cooling applications. Our direct numerical simulations (DNS) show that under certain heating conditions, measured by the buoyancy parameter C , shear turbulence may either be completely laminarised or transitions to a relatively quiescent convection-driven state. A linear instability is found at $C \approx 4$, roughly independent of the Reynolds number Re . Buoyancy forces cause a flattening of the mean streamwise velocity profile, an effect which in isothermal pipe flow has recently been linked to complete suppression of turbulence (Kühnen *et al.*, *Nat. Phys.*, vol. 14, 2018, pp. 386–390) and enhanced nonlinear stability (Marensi *et al.*, *J. Fluid Mech.*, vol. 863, 2019, pp. 50–875). In agreement with these findings, the lower-branch travelling-wave solution analysed here, which is believed to mediate transition to turbulence in isothermal pipe flow, is shown to be suppressed by buoyancy. Furthermore, the laminarisation criterion proposed by He *et al.* (*J. Fluid Mech.*, vol. 809, 2016, pp. 31–71), based on an apparent Reynolds number of the flow as measured by its driving pressure gradient, is found to capture the critical $C = C_{cr}(Re)$ above which the flow will be laminarised or switch to the convection-driven type. Bistability between shear and convection-driven states is thus observed in the region $4 \lesssim C \lesssim C_{cr}$ where the flow may or may not be laminarised depending on the initial flow of the experiment. Our analysis suggests that it is the weakened rolls, rather than the streaks, which appear to be critical for laminarisation.

Key words: Heated pipe flow

1. Introduction

Most energy systems rely on fluids to transfer heat from one device to another to facilitate power generation, provision of heating or production of chemicals. Flows are often forced through channels or arrays of pipes taking heat away from the surfaces. In a nuclear reactor, for example, the reactions occur within the fuel pins, which are cooled by flow of coolant through the channels formed by arrays of fuel pins to maintain their temperature within a specific limit as well as transferring energy to the steam generators. In an isothermal flow, the volume flux is driven by an externally applied pressure gradient, and the flow is referred to as ‘forced’. In a vertical configuration, however, buoyancy resulting from the lightening of the fluid close to the heated wall can provide a force that partially or fully drives the flow, referred to as mixed or natural convection, respectively.

† Email address for correspondence: elena.marensi@ist.ac.at

When heat flux is very high, we can have a ‘supernatural’ state of flow, where the buoyancy is sufficiently strong that volume flux is limited by an adverse pressure gradient. Under certain conditions (e.g. the Boussinesq approximation) an upward heated flow may be considered equivalent to a downward flow cooled at the boundary (Appendix A).

Mixed convection is of significant importance to engineering design and safety considerations and as such extensive research has been carried out to develop engineering correlations (Jackson *et al.* 1989; Yoo 2013), turbulence models (Kim *et al.* 2008; Bae 2016) and a better understanding of the physical flows (You *et al.* 2003). A particularly interesting physics is that the flow, at a Reynolds number where shear-driven turbulence is ordinarily observed, in the presence of buoyancy may be partially or fully laminarised, or becomes a convection-driven turbulent flow (i.e. natural convection, referred to above). Heat transfer may be significantly impaired under such conditions. He *et al.* (2016) (hereinafter referred to as HHS) modelled the effect of buoyancy using a prescribed body force, with linear or step radial dependence, without solving the energy equation. They attributed the suppression of turbulence to a reduction in the apparent Reynolds number of the flow, as measured by the pressure gradient required to drive the flow.

Meanwhile, in ordinary (isothermal) pipe flow, Kühnen *et al.* (2018) observed relaminarisation attributed to flattening of the base flow profile. The flattening was introduced by a range of internal and boundary flow manipulations. Marensi *et al.* (2019) showed the complement effect, i.e. the enhanced nonlinear stability of the laminar flow. They found that the minimal seed (smallest amplitude disturbance) for transition is ‘pushed out’ from the laminar state to larger amplitudes when the base flow is flattened, thus implying that a flattened base profile is more stable than the parabolic profile. Here, buoyancy forces also have a flattening effect. However, a clear link between the effect of buoyancy and the laminarisation phenomenon is still missing.

In this work, we are interested in whether a flow is turbulent or laminar under certain heating conditions and when a turbulent flow may be laminarised or vice versa under the influence of buoyancy. We address this question for a vertically heated pipe, initially in the dynamical systems context through linear stability and by investigating how travelling wave solutions are affected by the buoyancy force. Next, the statistical nature of the laminarisation is considered with reference to the ‘equivalent pressure-gradient’ analysis of HHS. In each case, we aim to elucidate the physical mechanisms underlying the buoyancy-suppression of turbulence, illustrating the bistability nature of such flows.

1.1. *Nonlinear dynamical systems view*

In subcritical wall-bounded shear flows, turbulence arises despite the linear stability of the laminar state (Drazin & Reid 2004; Schmid & Henningson 2001). In the last 30 years our understanding of transition to turbulence in such flows has greatly benefited from a fully nonlinear geometrical approach which adopts concepts from the dynamical systems theory. In this view, the flow is analysed as a huge (formally infinite-dimensional) dynamical system in which the flow state evolves along a trajectory in a phase space populated by various invariant solutions, travelling waves (TWs) and periodic orbits (POs). In shear flows with linearly stable laminar solutions, transition to turbulence occurs when a finite-amplitude perturbation to the system causes the flow state to cross the basin boundary (the so called “edge of chaos”) that separates initial conditions that lead to turbulence from those that decay and relaminarise (Itano & Toh 2001; Schneider & Eckhardt 2006). The disturbance of smallest amplitude on the laminar-turbulent edge is called the “minimal seed” for transition (Kerswell 2018).

Nonlinear travelling wave solutions were first discovered numerically in the early 1990s

for plane Couette flows (Nagata 1990) and in the 2000s for pipe flows (Faisst & Eckhardt 2003; Wedin & Kerswell 2004; Pringle & Kerswell 2007). Since then, partly thanks to the advances in our computational and experimental capabilities, a growing amount of evidence has been collected for their dynamical importance (see reviews Kerswell 2005; Eckhardt *et al.* 2007; Kawahara *et al.* 2012). These solutions, often referred to as “exact coherent states/structures” (ECSs), are believed to act as *organising centres* (Waleffe 2001) in phase space, in the sense that, when the flow state approaches them, spatio-temporally organised patterns (streaks and streamwise rolls) are observed (Hof *et al.* 2004; Kerswell & Tutty 2007). ECSs are finite-amplitude non-trivial solutions disconnected from the laminar state and enter via saddle-node bifurcations as the flow rate is increased. Some, typically those of higher spatial symmetry, exist at flow rates much below that at which transition is usually observed (Pringle *et al.* 2009). ECSs are linearly unstable, although with only a few unstable directions. They may be divided into ‘upper-branch’ and ‘lower-branch’ states, depending on whether they are associated with a high or low friction factor. Lower branch solutions are representative of the laminar-turbulent boundary and mediate transition to turbulence (Duguet *et al.* 2008; Schneider *et al.* 2007), while some upper-branch solutions are embedded in the turbulent attractor and are representative of the turbulent dynamics (Avila *et al.* 2013; Budanur *et al.* 2017).

Here, we are interested in studying how travelling wave solutions are affected by the buoyancy force in a vertical heated pipe and, in analysing their dynamics, we aim to elucidate the physical mechanisms underlying the buoyancy-suppression of turbulence. The transition between regimes is first investigated using linear stability in §3.2, followed by analysis of travelling waves in §3.3.

1.2. Equivalent pressure-gradient (EPG) analysis of HHS

HHS start with a fixed radially-dependent axial body force that models a buoyancy force. They observed that adding the force does not alter the turbulent viscosity of an isothermal flow driven by the same pressure gradient. In this respect, the body force-influenced flow has an equivalent reference flow, referred to as the EPG flow, whose Reynolds number is in turn referred to as the apparent Reynolds number of the former. The laminarisation of the body force-influenced flow is observed to be consistent with the reduction of the apparent Reynolds number. Further details of the analysis are provided in §3.4, and HHS prediction is compared with a suite of simulations in §3.5.

2. Formulation

Consider a vertically aligned circular pipe of diameter D , with the flow of fluid upwards. We model a section L of the pipe (figure 1(left)) and let $\{\mathbf{u}(\mathbf{x}, t), p(\mathbf{x}, t), T(\mathbf{x}, t)\}$ be the velocity, pressure and temperature fields, respectively. The fluid has kinematic viscosity ν , density ρ , volume expansion coefficient γ and thermal diffusivity κ . Under the Boussinesq approximation, density variations are ignored except where they appear in terms multiplied by the acceleration due to gravity, $g \hat{\mathbf{z}}$, leading to the governing equations

$$\nabla \cdot \mathbf{u} = 0, \quad (2.1)$$

$$\frac{\partial \mathbf{u}}{\partial t} + \mathbf{u} \cdot \nabla \mathbf{u} = -\frac{1}{\rho} \nabla p + \nu \nabla^2 \mathbf{u} + \frac{1}{\rho} (1 + \beta) d_z P \hat{\mathbf{z}} + \gamma g (T - T_{ref}) \hat{\mathbf{z}}, \quad (2.2)$$

$$\frac{\partial T}{\partial t} + \mathbf{u} \cdot \nabla T = \kappa \nabla^2 T - \epsilon, \quad (2.3)$$

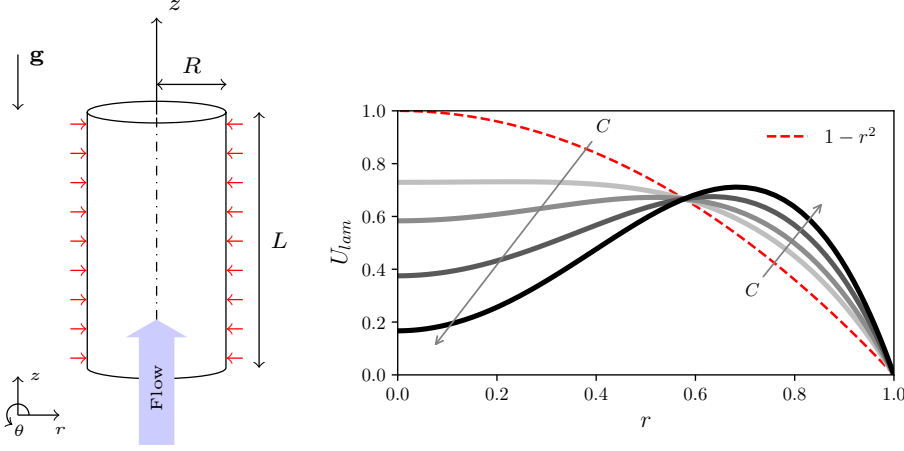


Figure 1: (Left) Schematic of the flow configuration. (Right) Laminar profiles as C is increased. Light grey to black lines: $C = 3, 5, 7.5, 10$.

where T_{ref} is a reference temperature to be defined in the next section, $d_z P$ is the pressure gradient for laminar flow with bulk velocity U_b , and $\beta(\mathbf{u})$ adjusts the pressure gradient to maintain fixed bulk velocity U_b when the flow changes. In the equation for T , the heating rate $\epsilon(t)$ appears as a heat sink term, which adjusts to maintain a fixed bulk value for T . We introduce axial periodicity, so that $\epsilon(t)$ may be considered equivalent to the rate at which heat absorbed by the fluid would otherwise be carried out of the section of pipe.

For laminar flow, the flow is purely axial so that radial heat transport is purely conductive. If ϵ_0 is the heating rate for the laminar case, then the observed quantity $Nu := \bar{\epsilon}/\epsilon_0$ is the Nusselt Number, where the overbar (\bullet) denotes time average.

2.1. Non-dimensionalisation

Let $T_{ref} = T_c$ be the centreline temperature for laminar flow, T_b be the bulk temperature, and T_w be the temperature at the wall. We choose the temperature scale $\Delta T = T_w - T_c = 2(T_w - T_b)$ and introduce the dimensionless temperature $\Theta = (T - T_c)/\Delta T$, such that the laminar temperature profile is $\Theta_{lam} = r^2$. Let the pipe radius $R = D/2$ be the length scale, and the isothermal laminar centreline velocity $2U_b$ be the velocity scale. Hereafter, all variables are dimensionless except $\epsilon(t)$ which always appears in the dimensionless ratio ϵ/ϵ_0 , i.e. the instantaneous Nusselt number. Non-dimensionalising with these scales, for the temperature equation we find

$$\frac{\partial \Theta}{\partial t} + \mathbf{u} \cdot \nabla \Theta = \frac{\kappa}{2U_b R} \nabla^2 \Theta - \frac{\epsilon R}{2U_b \Delta T}. \quad (2.4)$$

For the laminar case, $\Theta = \Theta_{lam} = r^2$, we find

$$0 = \frac{\kappa}{2U_b R} \cdot 4 - \frac{\epsilon_0 R}{2U_b \Delta T} \quad \text{i.e.} \quad \Delta T = \frac{\epsilon_0 R^2}{4\kappa}. \quad (2.5)$$

Plugging this ΔT back in to (2.4), we obtain the dimensionless temperature equation

$$\frac{\partial \Theta}{\partial t} + \mathbf{u} \cdot \nabla \Theta = \frac{1}{Re Pr} \nabla^2 \Theta - \frac{4}{Re Pr} \frac{\epsilon}{\epsilon_0}, \quad (2.6)$$

where $Re := U_b D / \nu$ is the Reynolds number and $Pr := \nu / \kappa$ is the Prandtl number. For the momentum equation we find

$$\frac{\partial \mathbf{u}}{\partial t} + \mathbf{u} \cdot \nabla \mathbf{u} = -\nabla p + \frac{1}{Re} \nabla^2 \mathbf{u} + \frac{4}{Re} (1 + \beta) \hat{\mathbf{z}} + \frac{\gamma g \Delta T R}{(2 U_b)^2} \Theta \hat{\mathbf{z}} \quad (2.7)$$

The coefficient of the buoyancy term can be written

$$\frac{\gamma g \Delta T R}{4 U_b^2} = \frac{1}{4} \frac{\gamma g (T_w - T_b) D^3}{\nu^2} \frac{\nu^2}{U_b^2 D^2} = \frac{1}{4} Gr Re^{-2}, \quad (2.8)$$

where $Gr := \gamma g (T_w - T_b) D^3 / \nu^2$ is the Grashof number. Although the Grashof number is in common use, from Gr it is difficult to judge the magnitude of the buoyancy force relative to the pressure gradient of the laminar flow for this particular configuration. We therefore write the dimensionless momentum equation as

$$\frac{\partial \mathbf{u}}{\partial t} + \mathbf{u} \cdot \nabla \mathbf{u} = -\nabla p + \frac{1}{Re} \nabla^2 \mathbf{u} + \frac{4}{Re} (1 + \beta + C \Theta) \hat{\mathbf{z}}, \quad (2.9)$$

where C measures the buoyancy force relative to the force that drives the laminar isothermal shear flow,

$$C = \frac{Gr / (4 Re^2)}{4 / Re} := \frac{Gr}{16 Re}. \quad (2.10)$$

The laminar velocity and laminar temperature profiles for this configuration are

$$U_{lam}(r) = (1 - r^2) + C \left(\frac{1}{3} r^2 - \frac{1}{4} r^4 - \frac{1}{12} \right), \quad \Theta_{lam}(r) = r^2, \quad (2.11)$$

and the no-slip and fixed-temperature boundary conditions at $r = 1$ are

$$\mathbf{u} = \mathbf{0}, \quad \Theta = 1, \quad (2.12)$$

respectively, while periodic boundary conditions are applied in the streamwise direction. The laminar velocity profiles for different C are shown in figure 1(right). For a statistically steady flow, Reynolds averaging is both time averaging and cylindrical surface averaging, where the latter is denoted as

$$\langle q \rangle(r) := \frac{1}{2\pi L} \int_0^L \int_0^{2\pi} q(\mathbf{x}) d\theta dz, \quad (2.13)$$

for $q = q(\mathbf{x})$ a generic scalar function of space. Turbulent fluctuations are calculated as deviations from the mean components of the flow, i.e. $\{\mathbf{u}'(\mathbf{x}, t), \Theta'(\mathbf{x}, t)\} := \{\mathbf{u}(\mathbf{x}, t), \Theta(\mathbf{x}, t)\} - \{\langle \mathbf{u} \rangle(r), \langle \Theta \rangle(r)\}$.

Simulations were carried out using the `Openpipeflow` solver (Willis 2017), appropriately modified to add the timestepping of the temperature field and include the buoyancy term in the momentum equation. A variable $q(r, \theta, z)$ is discretised using finite differences in the radial direction, with the points clustered near the wall, and Fourier decomposition in the azimuthal and streamwise directions, namely

$$q(r, \theta, z) = \sum_{k < |K|} \sum_{m < |M|} q_{km}(r_n) e^{i\alpha k z + m_p m \theta} \quad n = 1, \dots, N \quad (2.14)$$

where $\alpha = 2\pi/L$ is the streamwise wavenumber and m_p determines the azimuthal periodicity ($m_p = 1$ with no discrete rotational symmetries). At $Re = 5300$, in a $L = 5D$ long pipe we use a spatial resolution of $(N \times M \times K) = (64 \times 96 \times 96)$. The time step is dynamically controlled using the Courant–Friedrichs–Lewy (CFL) condition. The

isothermal pipe flow is recovered for $C = 0$ (no buoyancy force) and $Pr = 0$ (temperature diffuses immediately).

2.2. Travelling wave solutions

In order to apply dynamical systems theory, the discretised momentum and temperature equations are formulated as an autonomous dynamical system (Viswanath 2007; Willis *et al.* 2013a):

$$\frac{d\mathbf{X}}{dt} = \mathbf{F}(\mathbf{X}; \mathbf{p}), \quad (2.15)$$

where \mathbf{X} is the vector of dependent variables, here $\mathbf{X} = (\mathbf{u}, \Theta)$, and \mathbf{p} is the vector of parameters of the system, $\mathbf{p} = (Re, C)$. The simplest solution is an equilibrium, which satisfies $\mathbf{F}(\mathbf{X}; \mathbf{p}) = 0$. For pipe flow, the only equilibrium solution is the laminar solution. Travelling wave solutions satisfy $\mathbf{X}(\mathbf{x}, t) = g(ct) \mathbf{X}(\mathbf{x}, 0)$, where here $g(l)$ applies a streamwise shift by l , and c is the phase speed. Travelling waves are also known as ‘relative’ equilibrium solutions, as they are steady in a co-moving frame. They therefore satisfy

$$\mathbf{G}(\mathbf{X}(0), l, T) = g(-l)\mathbf{X}(T) - \mathbf{X}(0) = \mathbf{0}, \quad (2.16)$$

for some vector (\mathbf{X}, l, T) , and hence can be calculated via a root solving method. The most popular method at present is the Newton–Krylov method. (Note that in addition to (2.16), two extra constraints are required to match the extra unknowns l, T ; see Viswanath (2007)). Time-dependent periodic orbits may also be calculated by this method. Typically periodic orbits originate via a Hopf bifurcation off a travelling wave, but are not discussed further in this work.

Stability of the solutions is calculated using the Arnoldi method to solve the eigenvalue problem

$$e^{\sigma T} d\mathbf{X} = g(-l) (\mathbf{X}_0 + d\mathbf{X})(T) - \mathbf{X}_0(0), \quad (2.17)$$

where σ is the growth rate and the operator on the right hand side is linearised about the travelling wave \mathbf{X}_0 by taking $\|d\mathbf{X}\| \ll \|\mathbf{X}_0\|$. (Numerical performance is improved by replacing $\mathbf{X}_0(0)$ with $g(-l) \mathbf{X}_0(T)$ in (2.17)).

The Newton-Krylov and Arnoldi solver, already available as a utility of `Openpipeflow` (Willis 2017), were integrated with the time-stepping code described above for heated pipe flow.

3. Results and discussion

All results presented herein pertain to the case $Pr = 0.7$ and constant volume flux. This relatively low Prandtl number is a reasonable starting choice for the applications we are interested in, where most gasses have $Pr \approx 0.7$, e.g. CO_2 . In large scale cooling applications using liquid metal, Pr is much smaller. Cases where $Pr > 1$ (e.g. $Pr = 7$ for water) are more expensive numerically due to a need for higher resolution for the temperature field.

3.1. Direct Numerical Simulations

Simulations were performed in a pipe of length $L = 5D$ for a range of Reynolds numbers to study the effect of the buoyancy parameter C . Results are first shown for a relatively low Reynolds number, $Re = 2500$. Figure 2 shows complete relaminarisation of transitional turbulence in response to the introduction of buoyancy for intermediate values of $C = \mathcal{O}(10^{-1}) - \mathcal{O}(1)$. Relaminarisation events are revealed by monitoring the energy of the streamwise-dependent component of the flow, denoted E_{3D} , which shows a rapid

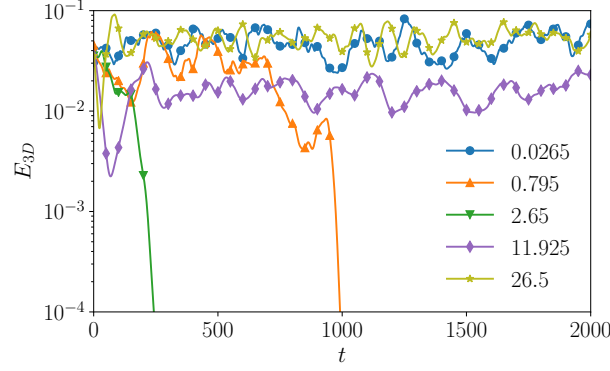


Figure 2: Energy of the streamwise-dependent component of the flow. $Re = 2500$, $L = 5D$, $Pr = 0.7$ for a range of C . Intermediate C destabilise the turbulence, or even cause immediate relaminarisation.

decay when the flow relaminarises, $E_{3D} \rightarrow 0$ and $\varepsilon(t)/\varepsilon_0 \rightarrow 1$. At larger $C \geq \mathcal{O}(10)$, turbulent fluctuations are not completely suppressed. Instead a convection-driven flow is set up, which becomes stronger as C is increased.

At $Re = 5300$ the effect of buoyancy is found to be slightly different – turbulence is not observed to undergo complete relaminarisation, but instead transitions directly to a weak convection-driven state. Figure 3 shows simulations with $C = \mathcal{O}(1) - \mathcal{O}(10)$. The buoyancy causes suppression of the turbulence and therefore a drop in $\varepsilon(t)/\varepsilon_0$, so that the Nusselt number $Nu = \bar{\varepsilon}/\varepsilon_0$ reduces substantially. The corresponding velocity and temperature mean profiles, $\langle u_z \rangle(r)$ and $\langle \Theta \rangle(r)$, are shown in bottom graphs of figure 3 together with the laminar profiles at $C = 0$ for comparison. Cases where turbulence is suppressed exhibit a flattened base velocity profile.

The case for $C = 7.5$ is shown for longer time in figure 4(left). The shear-driven turbulent state is metastable only, and around $t \approx 2000$ turbulence is more suppressed as there is a switch to the more quiescent convection-driven state. As C is increased further the buoyancy starts to drive a more turbulent convection-driven state. For these cases the velocity profile is more ‘M-shaped’ as seen in figure 4(right).

Figure 5 shows the type of state seen in simulations, laminar flow (L), shear-driven turbulence (S) and convection-driven flow (C), for a range of Re and C . The initial condition for each simulation was a previously calculated shear-driven state at similar Re . (This is except for $Re \leq 2000$ and $C > 3$, where it is clear that the shear-driven state is not supported, and hence the initial condition was of convection type). For each simulation it is relatively easy to distinguish between the shear- and convection-type flows, since the former shows far more chaotic time series and higher heat flux. The case for $C = 7.5$ in figure 4(left) shows this difference, and also that multiple behaviours are possible at the same parameters for significant periods of time. The meta-stable shear-driven state is marked if observed for $\gtrsim 1000$ time units. A relaminarisation is marked if the energy of the streamwise component of the flow drops below 10^{-5} . For the isolated case where this occurred with $C = 6$, a weak convective flow develops for a different initial condition. Overall, figure 5 indicates that, as C (or Gr) increases, a larger Re is needed in order to drive shear turbulence, or, equivalently, as Re increases, shear-driven states persist to larger C . For $C \geq 4$ simulations suggest that a convective instability kicks in, roughly independently of the Reynolds number over this range. In between, it is possible to completely relaminarise flow up to $Re \approx 3500$, but at larger Re the progression is as

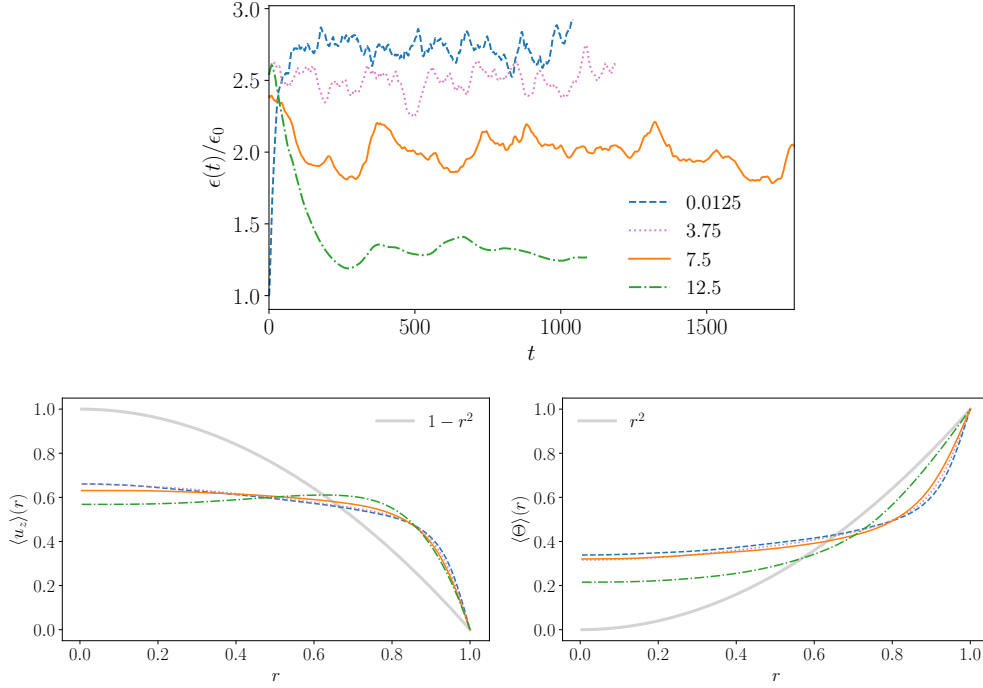


Figure 3: $Re = 5300$, $L = 5D$, $Pr = 0.7$, resolution $64 \times 96 \times 96$. Top: Normalised instantaneous heat flux, $Nu = \epsilon/\epsilon_0$. Bottom: Snapshots of $\langle u_z \rangle(r)$ and $\langle \Theta \rangle(r)$.

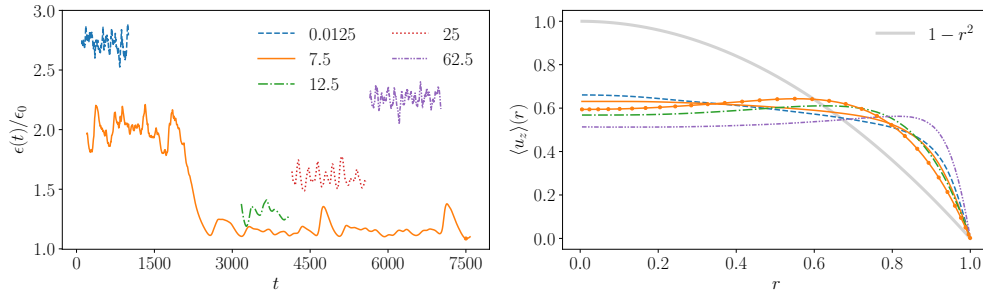


Figure 4: Parameters as in figure 3 but for larger C . Left: Normalised instantaneous heat flux, $Nu = \epsilon/\epsilon_0$ (the offset in time is for clarity only). Right: Snapshots of $\langle u_z \rangle(r)$. The profile at $C = 25$ is omitted for clarity.

in figure 4 – from a shear-driven turbulent state to a weak convection-driven state, then to a more turbulent convection-driven state as C is increased.

In the following sections we determine whether the boundaries of stability observed in figure 5 are consistent with linear stability of the laminar flow, analysis of travelling wave solutions and the viewpoint of HHS.

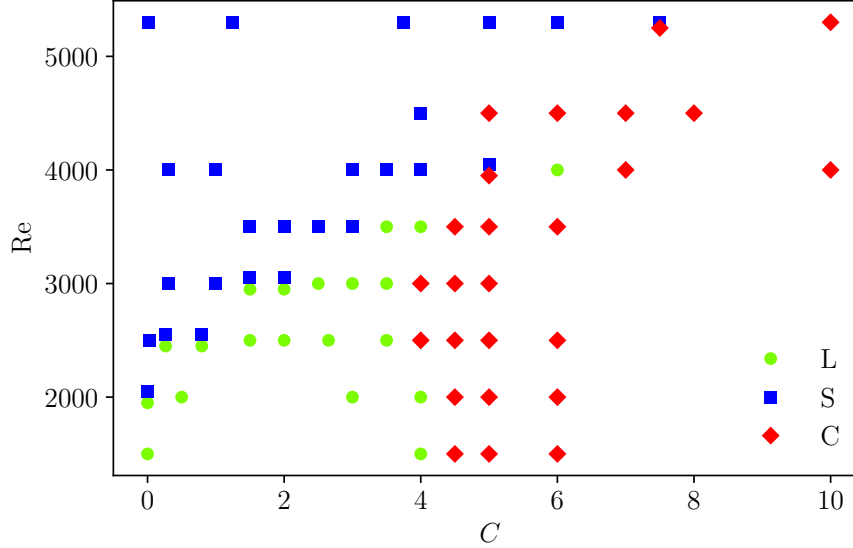


Figure 5: Regions of laminar (L) flow, shear-driven (S) turbulence and convection-driven (C) flow. Points where multiple behaviours are observed are marked with a slight offset in Re .

3.2. Linear stability analysis

As the transition to shear-driven turbulence in isothermal flow occurs in the absence of a linear instability, this section relates to the transition to convection-driven flow states, in particular with respect to loss of stability of the laminar base (2.11) for non-zero C .

Linear stability analysis is performed for a fixed streamwise wavenumber $\alpha = 1.7$, $k = 1$ and for azimuthal wavenumbers $m = 1$ and 2. Neutral curves, where the growth rate $\Re(\sigma) = 0$, are shown in figure 6. As expected, the $m = 1$ mode is found to be the least stable, since it corresponds to the spatially largest mode. It exhibits fairly complex dependence on C , however. Consistent with the linear stability of isothermal pipe flow, the critical Reynolds number approaches infinity as $C \rightarrow 0$ for any m .

Consistent with the appearance of the convective state found in simulation (figure 5), at $C \approx 4$ a linear instability appears, roughly independent of Re for most of the range considered. The corresponding laminar profiles for $C = 3-10$ are shown in figure 1(right). For $C > 4$ the profiles present an “M-shape” (independent of Re , see (2.11)), which becomes increasingly more pronounced as C increases. The difference at the centreline is more than 80% for $C = 10$. The profile at $C = 3$ is flatter than the parabolic (isothermal) profile, with a centreline difference of almost 30%, but does not have any inflection point.

Figure 6 also shows that, for $C \gtrsim 4$, a region of restabilisation is observed as Re is increased. This is also evidenced in figure 7, which shows a region of negative $\Re(\sigma)$ for $1450 < Re < 6200$ at $C = 5$. This region is likely to account for the outlying relaminarisation that occurred in figure 5 at $Re = 4000$, $C = 6$. Isosurfaces of streamwise vorticity for the eigenfunctions corresponding to the two neutral points where $\Re(\sigma)$ becomes positive are also shown in the insets of figure 7. For the larger $Re \approx 6200$ the eigenfunction looks like it is spiralling in the centre and resembles the “spiral” solution found by Senoo *et al.* (2012), although their visualised solutions are nonlinear.

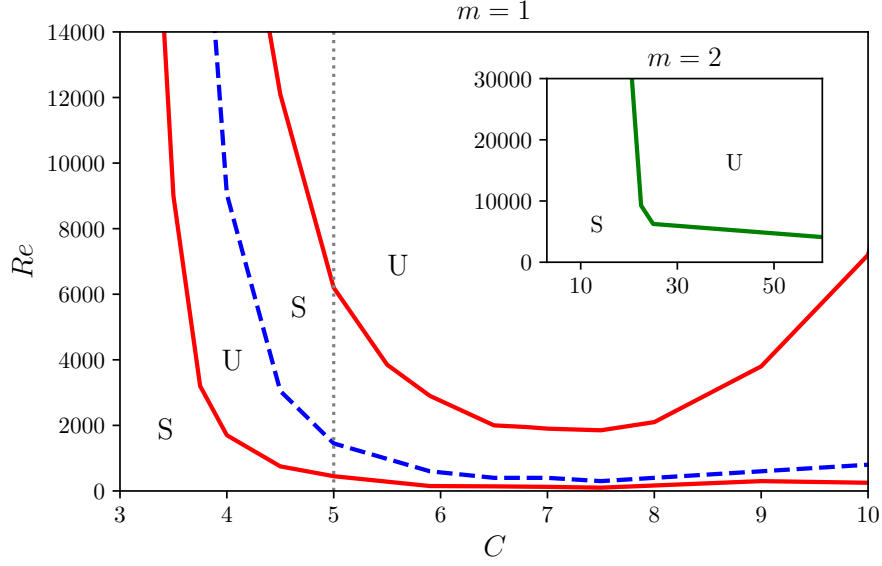


Figure 6: Linear stability analysis for $m = 1$, $\alpha = 1.7$, $k = 1$, ($L = 1.85D$). Inset: $m = 2$.

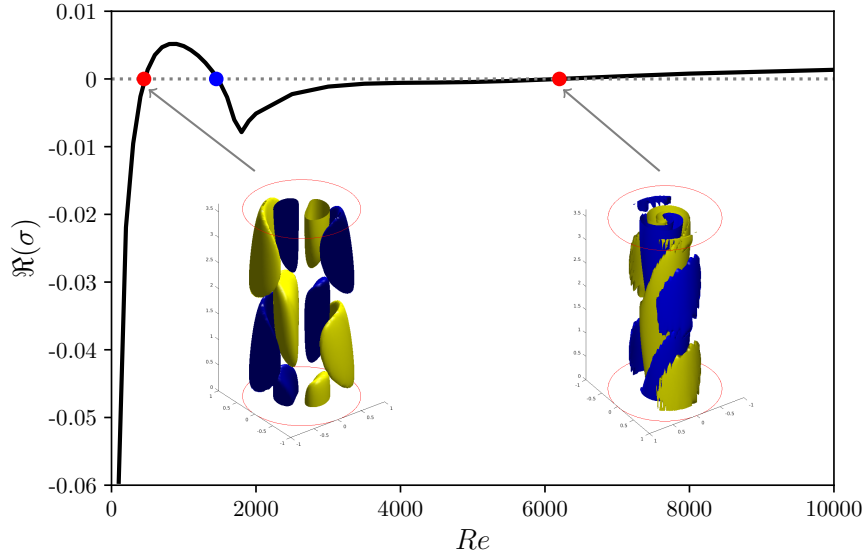


Figure 7: Growth rate vs Reynolds number, $m = 1$, $\alpha = 1.7$, $k = 1$, ($L = 1.85D$) and $C = 5$. Insets: streamwise vorticity (blue/yellow are 30% of the min/max value) close to the two neutral points ($Re \approx 400$ and 6200).

3.3. Continuation from TW_{N4L}

To better understand the effect of buoyancy, we perform a nonlinear analysis, starting from a known TW in isothermal pipe flow ($C = Gr = 0$) and continuing the solution to larger values. A vast repertoire of TWs has now been compiled in isothermal pipe flows

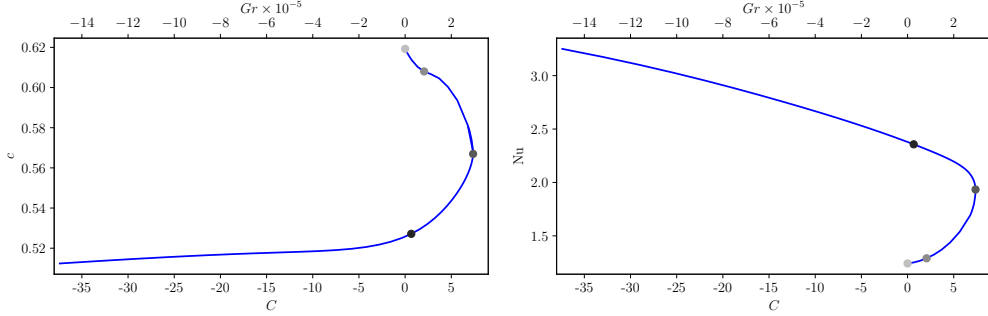


Figure 8: Continuation in C (or Gr) from N4L ($Re = 2500$, fixed flux). (a) Phase speed c vs C (or Gr), (b) Nu vs C (or Gr). Circles indicate the points along the continuation at which mean streamwise velocity and temperature profiles are shown in figure 9.

(Budamur *et al.* 2017). For our purpose we decided to focus on a fundamental solution, off which others are found to bifurcate, and which is characterised by relatively smooth continuation branches. The chosen TW is a highly-symmetric (satisfying both shift-reflect and shift-rotate symmetries, see Willis *et al.* (2013b)) and belongs to the so-called ‘N-class’ (Pringle *et al.* 2009). Following Willis *et al.* (2016) we start with the ‘minimal flow unit’ at Reynolds number $Re = 2500$ with domain $(r, \theta, z) = [0, 1] \times [0, \pi/2] \times [0, 2\pi/1.7]$, i.e. $m_p = 4$ and $\alpha = 1.7$ in (2.14). Adopting the nomenclature of Pringle *et al.* (2009), we refer to this solution as TW_{N4L} .

For isothermal flow ($C = Gr = 0$), the phase speed of TW_{N4L} is $c = 0.61925$. The isothermal TW was first reconverged at $Pr = 0.7$ using the Newton solver. A parametric continuation in C to non-zero values was then performed (figure 8) for fixed Re , Pr and α . We were able to continue the isothermal solution from $C = 0$ around positive C and find that it connects with the upper branch at $C = 0$, then beyond to $C \approx -40$. (Negative C corresponds to a downward cooled flow; Appendix A). As a check, we verified that the values of $c = 0.52575$ and $Nu = 2.378$ at $C = 0$ on the upper branch, as well as the mean profiles, matched those of the previously known upper-branch isothermal solution TW_{N4U} with $Pr = 0.7$.

In figure 8(right) it is seen that from $C = 0$ to $C = 6$ the Nusselt number Nu increases by approx 0.75. By comparison, along the upper branch, over the large range $C = 6$ to $C = -40$, it increases by only a further 1.25. Relatively speaking, the lower branch is rapidly pushed back towards the upper branch over the increase in C , and is suppressed altogether for $C > 7.5$. The mean velocity and temperature profiles at different points along the continuation are shown in figure 9. Observe that the profile in the near-wall region, where rolls and streaks occur, is similar at the saddle-node point (SN) to that of the isothermal upper branch (UB) solution. Figure 10(left) shows these rolls (arrows) and streaks (contours) in cross sections of the velocity perturbation at the saddle-node point. The corresponding temperature perturbation field (‘thermal streaks’) is shown on the right. There is no obvious difference of the velocity perturbation from its isothermal counterpart in the near wall region, while the core shows a strongly decelerated region relative to the (isothermal) laminar profile.

Continuations were also performed at $Re = 2000$ and 3000 , after reconverging the isothermal TW_{N4L} at these Reynolds numbers. Results are shown in figure 11. The TW survives to larger C as the Reynolds number increases (the saddle-node point of each curve moves to larger C as Re increases). This is consistent with the shear turbulence

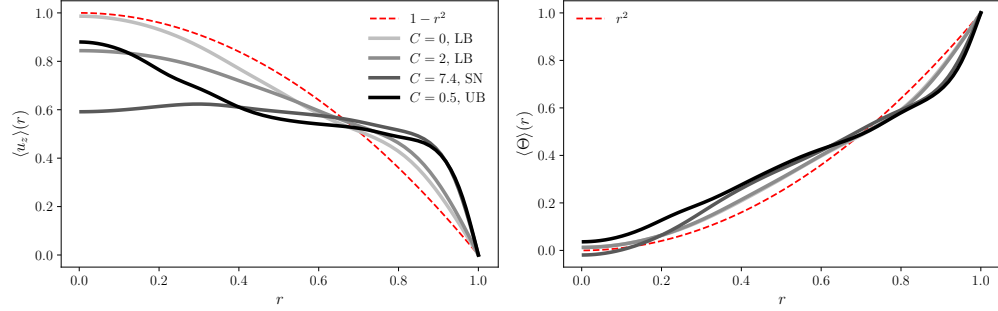


Figure 9: Mean streamwise velocity and temperature profiles at the points along the continuation from N4L ($Re = 2500$, fixed flux) marked in figure 8. The temperature profiles for $C = 0$ and $C = 2$ on the lower branch are indistinguishable.

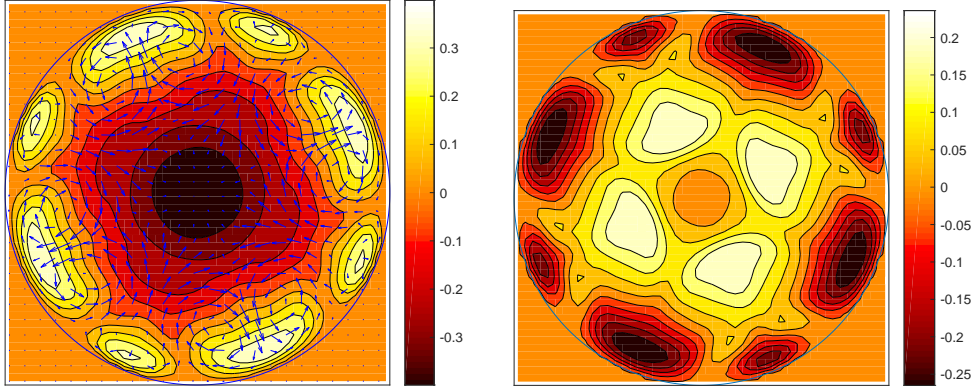


Figure 10: Cross sections of streamwise velocity (left) and temperature (right) perturbations (deviations from the isothermal laminar flow) for the N4L travelling wave at $Re = 2500$ and $C = 7.4$ (saddle node). Ten contours are used between the maximum and minimum. The arrows in the left graph indicate cross-sectional velocities

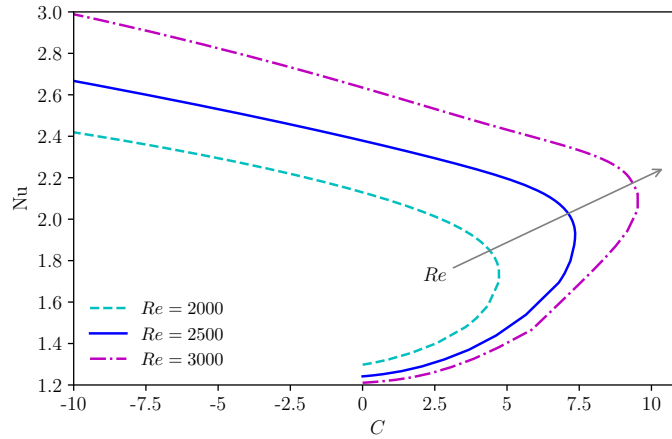


Figure 11: Continuation in Gr (or C) from N4L (fixed flux) at $Re = 2000$, 2500 and 3000 .

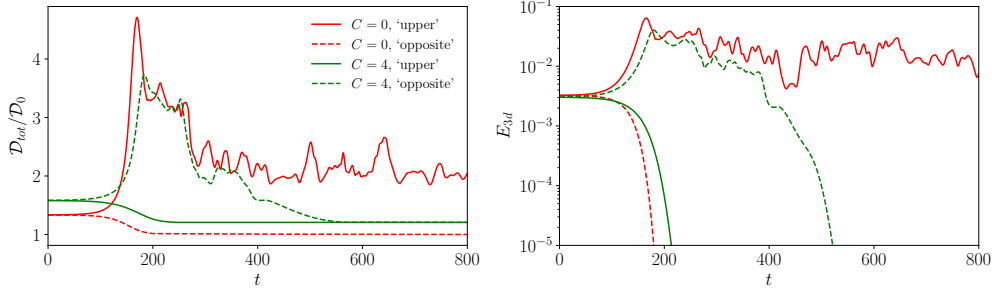


Figure 12: Times series of (left) total dissipation \mathcal{D}_{tot} (normalised by the laminar isothermal value $\mathcal{D}_0 = 2\pi L_z | -2| = 4\pi L_z$) and (right) energy of the streamwise-dependent modes E_{3d} for simulations started from the lower-branch TW solutions at $Re = 3000$, $\alpha = 1.7$ with $C = 0$ and $C = 4$. The TW is perturbed by adding $\mp 0.001(\mathbf{w}_1 + 0.01\mathbf{w}_2)$ (denoted as ‘upper’ and ‘opposite’ directions) where \mathbf{w}_1 and \mathbf{w}_2 are the first (leading) and second eigenvectors. Shooting in the ‘upper’ direction leads to turbulence for $C = 0$, while the flow goes back to laminar when perturbed in the opposite direction. For $C = 4$ both directions end up at the laminar point.

region in figure 5 persisting to larger C as Re is increased. The saddle-node bifurcations at each Re occur at much larger values of C than those at which suppression of turbulence was observed in the DNS. For example, at $Re = 2500$ the saddle-node bifurcation occurs at $C \approx 7.5$, while in figure 5 shear-turbulence survives only for $C \lesssim 1$. This is not so surprising, considering that in isothermal pipe flows the lowest Re at which an ECS was found ($Re = 773$) is much below the commonly observed value for transition in experiments ($Re \approx 1800 - 2300$). Furthermore, it should be taken into account that only one TW solution is analysed here – it cannot capture the entire phenomenon of turbulence suppression in a heated pipe flow, although is found to capture some of the fundamental characteristics.

Figure 12 shows that, while the lower branch solution for $Re = 3000$ is on the edge of an attractor for shear-driven turbulence at $C = 0$, this is no longer the case for $C = 4$. Shear-driven turbulence does not survive in the heated case, although shooting in the upper direction for $C = 4$ does still produce a short turbulent transient. In particular, large amplification of the initial disturbance still occurs in the heated case, but the self-sustaining mechanism appears to be disrupted.

To summarise this section, we have observed that TW solutions are suppressed and that they are connected to the transition *to* turbulence. The observations are consistent with destabilisation of the shear-driven turbulent state, but at this stage another approach is required to forge an approximate quantitative link with the transition *from* turbulence.

3.4. Calculation of the apparent Reynolds number of HHS

HSS studied the suppression of turbulence in pipe flow in the presence of a prescribed radially-dependent (streamwise and spanwise independent) streamwise body force that mimics the buoyancy force in mixed convection. Following careful analysis of the resulting flows, they proposed a new perspective on the flow relaminarisation. Here we summarise the key points of their analysis and apply it to a selected example case from our data. (The interested reader is referred to sections 3.3 and 3.5 of HHS for a detailed derivation.) In the following section we relate HHS analysis to the phase diagram determined from the simulations of §3.1.

The analysis starts by decomposing the body-force influenced flow (i.e. the total flow) into a pressure-driven flow of equivalent pressure gradient (the EPG reference flow) and

a perturbation flow due to the body force. In contrast to the conventional view, HHS observe that adding a body force to a flow initially driven only by a pressure gradient does not alter its turbulent mixing characteristics and in particular the turbulent viscosity remains approximately the same. From this point of view, the body-force influenced flow behaves in the same way as the EPG flow and relaminarisation occurs when the Reynolds number Re_{app} of this ‘apparent’ flow drops below a certain threshold (a nominal value of 2300 was selected). By writing the bulk velocity U_b of the EPG flow (denoted hereinafter with †) as the difference between that of the total flow and of the body-force perturbation driven flow (indicated with a superscript ‘f’), i.e. $U_b^\dagger = 0.5 - U_b^f$, the above relaminarisation criterion can be expressed as

$$Re_{app} := Re(1 - 2U_b^f) < 2300. \quad (3.1)$$

To determine U_b^f , the following expression was derived by integrating three times the Reynolds-averaged z -momentum equation of the body-forced perturbation flow:

$$U_b^f := Re \left[\underbrace{\frac{1}{2} \int_0^1 (1 - r^2) f(r) r dr}_{\mathcal{I}_1} + \underbrace{\int_0^1 r \mathcal{R}_{uv}^f(r) r dr}_{\mathcal{I}_2} \right] \quad (3.2)$$

where $\mathcal{R}_{uv}^f(r) := \overline{\langle u'_z u'_r \rangle^f}$ is the Reynolds shear stress due to the perturbation flow induced by the body force $f(r)$. The first integral of (3.2) represents the direct contribution of the body force (which is assisting the flow), while the second integral corresponds to the turbulent contribution related to the body-force perturbed flow. The Reynolds stress term \mathcal{R}_{uv}^f of the body-force perturbed flow is related to that of the total and EPG flows via the decomposition introduced earlier and is evaluated by introducing the eddy viscosity concept, under the assumption that the eddy viscosity ν_t of the total flow is the same as that of the EPG flow, ν_t^\dagger . The following expression is then obtained

$$\mathcal{R}_{uv}^f(r) = -\frac{\nu_t^\dagger}{Re} \frac{d\mathcal{W}_z^f}{dr}, \quad (3.3)$$

where the perturbation flow $\mathcal{W}_z^f(r) := \overline{\langle u_z \rangle^f}$ due to the imposed body force is obtained by integrating the Reynolds-averaged z -momentum equation

$$0 = \frac{1}{r} \frac{d}{dr} \left[\frac{r}{Re} \left((1 + \nu_t^\dagger) \frac{d\mathcal{W}_z^f}{dr} \right) \right] + f, \quad (3.4)$$

provided that the EPG flow (and hence ν_t^\dagger) is known. Equations (3.3) and (3.4) correspond to equations (3.6) and (3.7) of HHS and the reader is referred their sections 3.3 and 3.5 for a detailed derivation.

Here, we apply the criterion for relaminarisation (3.1) proposed by HHS to our model for a vertical heated pipe. The radially dependent body-force is $f_0 = (4C/Re)\langle\bar{\Theta}\rangle(r)$. Since the body-force in HHS is zero at the axis, we shift the temperature profile by its value at the axis $\langle\bar{\Theta}\rangle|_{r=0}$ and absorb this constant into the pressure gradient (see figure 13). This leads to the body force

$$f_1(r) = (4C/Re) \left[\langle\bar{\Theta}\rangle - \langle\bar{\Theta}\rangle|_{r=0} \right] \quad (3.5)$$

and a fixed-pressure Reynolds number

$$Re_p = Re \left[(1 + \beta) + C \langle\bar{\Theta}\rangle|_{r=0} \right]$$

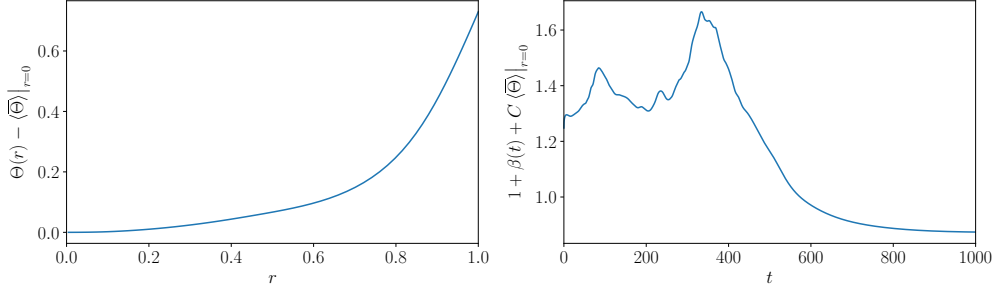


Figure 13: Application of HHS's relaminarisation criterion (3.2) in the case $C = 2$ and $Re = 3000$. Left: Temperature profile shifted by $\langle \Theta \rangle|_{r=0}$. Right: the corresponding pressure gradient.

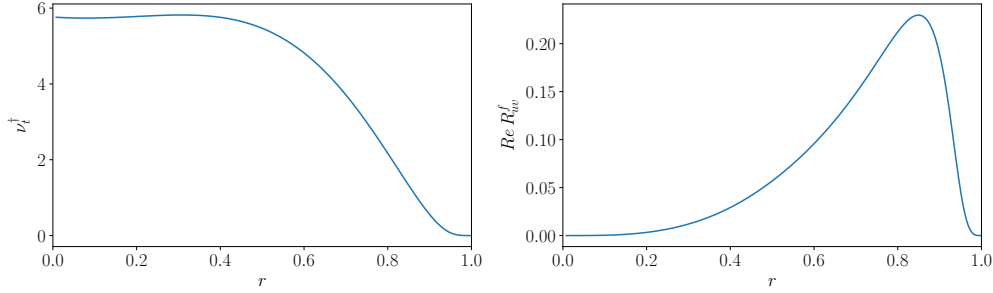


Figure 14: Eddy viscosity and associated Reynolds shear stress of the EPG flow in the case $C = 2$ and $Re = 3000$. The eddy viscosity is calculated following an approach similar to Willis *et al.* (2010), as summarised in Appendix B.

Initially, we consider the simulation with $C = 2$ and $Re = 3000$ for which it is observed that $Re_p = 4252.71$. By inserting $f = f_1$ in \mathcal{I}_1 we obtain $Re \mathcal{I}_1 = 0.12$.

To calculate \mathcal{I}_2 we need to evaluate the EPG flow in order to obtain $\nu_t^\dagger(r)$. By definition, $Re_p^\dagger = Re_p$. In an approach similar to Willis *et al.* (2010), summarised in Appendix B, the eddy viscosity $\nu_t^\dagger(r)$ of the EPG reference flow is calculated using an expression originally suggested by Cess (1958). The resulting eddy viscosity is shown in figure 14(left). Using the assumption $\nu_t = \nu_t^\dagger$ and expressions (3.3) and (3.4), we evaluate the Reynolds stress \mathcal{R}_{uv}^f (see figure 14(right)) and inserting it in (3.2) we obtain $Re \mathcal{I}_2 = 0.0405$. Putting everything together, (3.2) gives $U_b^f = 0.1594$. Then, $Re_{app} = Re(1 - 2U_b^f) = 2043.7 < 2300$, i.e. the flow is expected to relaminarise. This value obtained for the apparent Reynolds number is reasonable, since relaminarisation occurs after approximately 400 time units (see figure 13 (right)).

3.5. HHS prediction of phase diagram and nonlinear dynamics

We now consider the general case of a flow at Re with heating C , while introducing a number of approximations to simplify the analysis.

Firstly, the case discussed in §3.4 suggests that $Re \mathcal{I}_1$ has a significantly greater contribution than $Re \mathcal{I}_2$ in determining the body-force perturbation flow. This is found to be generally true for the cases considered herein, as well as those discussed in HHS, and hence we omit the term $Re \mathcal{I}_2$ for simplicity below. The perturbation flow due to the

body force can thus be evaluated as

$$U_b^f \approx Re \mathcal{I}_1 = \frac{1}{2} Re \int_0^1 (1-r^2) f(r) r dr = 2C \int_0^1 (1-r^2) [\langle \bar{\Theta} \rangle - \langle \bar{\Theta} \rangle|_{r=0}] dr, \quad (3.6)$$

where (3.5) has been used for $f(r)$.

Secondly, figure 3(bottom right) shows that the temperature mean profiles are remarkably similar in all turbulent shear-driven flows (i.e. ignoring the laminar or convection driven flow states), as far as the integral part of the right-hand side of (3.6) is concerned, despite that the values of the Nu (proportional to the gradient at the wall) are necessarily quite different for different cases. For the case $Re = 5300$ $C = 3.75$, for the left-hand side of (3.6) we obtain $Re \mathcal{I}_1 = 0.164$. By applying the above assumption,

$$U_b^f \approx Re \mathcal{I}_1 = \frac{0.164}{3.75} C = 0.04 C \quad (3.7)$$

Let $Re_{app}=2300$ to find the critical C for flow laminarisation, that is,

$$Re(1 - 2U_b^f) = Re(1 - 0.08 C) = 2300 \quad (3.8)$$

or

$$C_{cr,1} = 12.5 \left(1 - \frac{2300}{Re} \right). \quad (3.9)$$

For $C \gtrsim C_{cr,1}$ we expect to see rapid transition from the shear-driven turbulent state to the convective state. Noting $C = Gr/(16Re)$, the above can be expressed as a critical Grashof number:

$$Gr_{cr,1} = 200(Re - 2300) \quad (3.10)$$

Let us now consider the opposite scenario in which the flow under heating C is either laminar or convection driven. Figure 3(bottom right) shows that the temperature profiles in such flows are significantly different from those in a turbulent shear-driven flow, and generally with a much thicker thermal boundary layer, and hence a greater buoyancy force. Consider the extreme case when the radial heat transfer is purely due to conduction and the temperature distribution is given by $\langle \bar{\Theta} \rangle = r^2$. The buoyancy-driven perturbation flow is therefore

$$U_b^f \approx Re \mathcal{I}_1 = 2C \int_0^1 (1-r^2) r^2 dr = \frac{C}{6} \quad (3.11)$$

Then a second critical $C = C_{cr,2}$ can be evaluated,

$$C_{cr,2} = 6 \left(1 - \frac{2300}{Re} \right), \quad (3.12)$$

below which the flow is expected to transition to the shear-driven turbulent flow. To put it another way, it is predicted that metastability of the shear-driven turbulent state should *not* be observed for $C \lesssim C_{cr,2}$. Between $C_{cr,1}$ and $C_{cr,2}$ the shear-driven state is expected to be meta-stable, so that this, or a convective state, may be observed. In terms of the Grashof number,

$$Gr_{cr,2} = 96(Re - 2300). \quad (3.13)$$

Equations (3.9) and (3.12) are plotted on the $Re - C$ graph in figure 15 together with all DNS results already presented in figure 5. The data of figure 5 was obtained starting from shear-driven turbulent states. Some additional simulations were performed at $Re = 5300$ starting from convection-driven states and are reported in figure 15 using

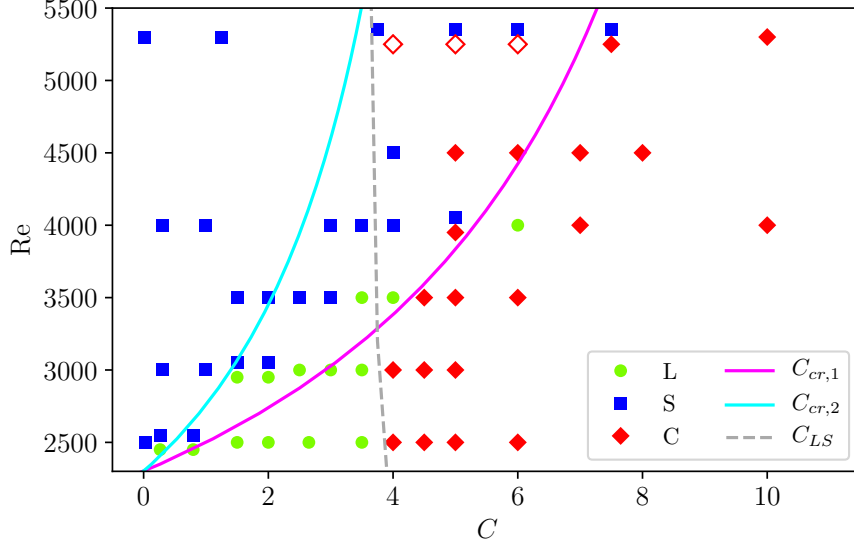


Figure 15: Regions of laminar (L) flow, shear-driven (S) turbulence and convection-driven (C) flow, as in 5, together with equations (3.9) and (3.12) and the linear stability stability curve. Initial conditions are a shear-driven turbulent state, except for the hollow symbols at $Re = 5300$ which are started with a convection driven state, and similarly cases towards the bottom-right, where it is clear that the shear-driven state decays immediately.

hollow symbols, with a slight offset in Re for visualisation reasons. Note that in a $Re-Gr$ graph (3.10) and (3.13) are straight lines.

Considering a series of DNS runs for a fixed Re , for example $Re = 5300$, but increasing C values (heating) starting from $C = 0$, equation (3.9) gives the critical $C = C_{cr,1}$ above which the flow will be laminarised or switch to convection-driven. On the other hand, starting from a large C when the flow is laminarised or convective, equation (3.12) predicts a critical $C = C_{cr,2}$ below which the flow will be turbulent when sufficient disturbances are provided in the DNS. As $C_{cr,1}$ is larger than $C_{cr,2}$ for a given Re , there is an overlap in the possible state of flow, and consequently there is a hysteresis region in which the flow may or may not be laminarised, depending on the initial flow of the simulation (or experiment). As a result, the $Re-C$ plane can be divided into three regimes by the curves representing the two equations, i.e., turbulent shear-driven flow (regime I), convection-driven or laminar flow (regime III) and regime II in which either of the above may happen dependent on the initial flow. Note that for the Reynolds number range considered here, the linear stability curve (showed as a dashed grey line in figure 5) is always to the right of $C_{cr,2}$, i.e. $C_{cr,2} < C_{LS}$. The two curves cross at $Re \approx 6000$ (not shown), which means that, for $Re < 6000$ the convective flow is always linearly stable if $C < C_{cr,2}$. Hence, below $Re \approx 6000$, shear driven turbulence may be observed for $C < C_{LS}$.

A plot showing the phase transitions for the fixed Reynolds number $Re = 5300$ is provided in figure 16, where the Nusselt number is displayed as a function of C for simulations started with either shear-driven or convection-driven states. The two critical C at this Reynolds number, $C_{cr,1} = 7.1$ and $C_{cr,2} = 3.4$, are indicated with vertical lines in figure 16. Starting from an unheated ($C = 0$) turbulent flow, applying a low

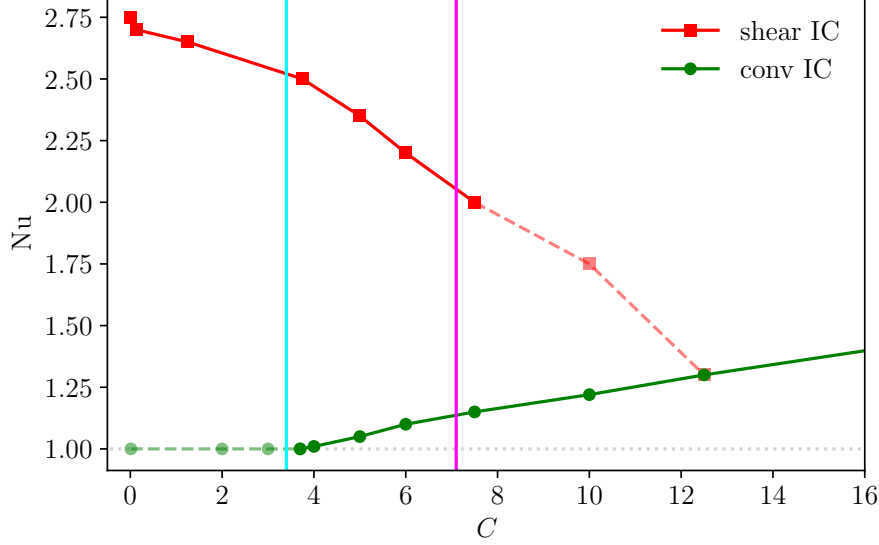


Figure 16: Nusselt number vs C for simulations started with shear and convection initial conditions at $Re = 5300$.

heating ($C \lesssim 7$), we observe that the flow remains turbulent over the entire period of simulation. The dynamics thus sits on the upper branch shown in figure 16. As C is increased, the lifetime of shear-turbulence seems to drop below 2000 time units for $C \geq 7.5$ and turbulence only survives for less than 500 time units at $C = 10$. It then switches to the convection-type flow. This behaviour is marked in figure 16 by plotting the upper-branch curve with a dashed line for $C \geq 7.5$ until it crosses the lower-branch at $C = 12.5$. At this value of C , indeed, the switch to the convective flow appears to be immediate. Now, starting from this convection-driven flow and applying a lower C , the flow remains convection-driven turbulent for $C \geq 3.8$, or relaminarises for $C \lesssim 3.8$. This value of C corresponds to the onset of the linear instability, which is responsible for the kink in Nu as C is decreased. Our previous analysis predicts that for flows on the left of (3.12), their Re_{app} is greater than 2300, hence they may be prone to transition to turbulence subject to sufficient disturbances. Correspondingly, the lower-branch curve in figure 16 is plotted with a dashed line for $C < C_{cr,2} = 3.4$ to indicate that in practice (e.g. in a lab experiment) the flow would become shear-driven turbulent again. However, as previously discussed, at this Reynolds number, $C_{cr,2} < C_{LS}$. Bistability (between shear or convection driven states) is thus observed for $3.8 \lesssim C \lesssim 7.5$. The latter value is in very good agreement with the threshold $C_{cr,1} = 7.1$ predicted above.

In figures 17 and 18 the turbulent structures of the isothermal and heated flows at $Re = 5300$, $C = 0$ and 5, are compared to those of the EPG reference flow. The latter was computed by performing a DNS with fixed pressure gradient such that $Re_p^\dagger = Re_p = 10898.7$. The flow structures - streaks and vortices - are visualised as isosurfaces of streamwise velocity and streamwise vorticity fluctuations, normalised by the apparent friction velocity based on the pressure gradient component of the wall shear stress only, $u_{\tau p}^*$, where the asterisk $*$ denotes a dimensional quantity here. The resulting apparent friction Reynolds number is $Re_{\tau p} := u_{\tau p}^* R^* / \nu^* = Re_\tau^\dagger = 147.6$.

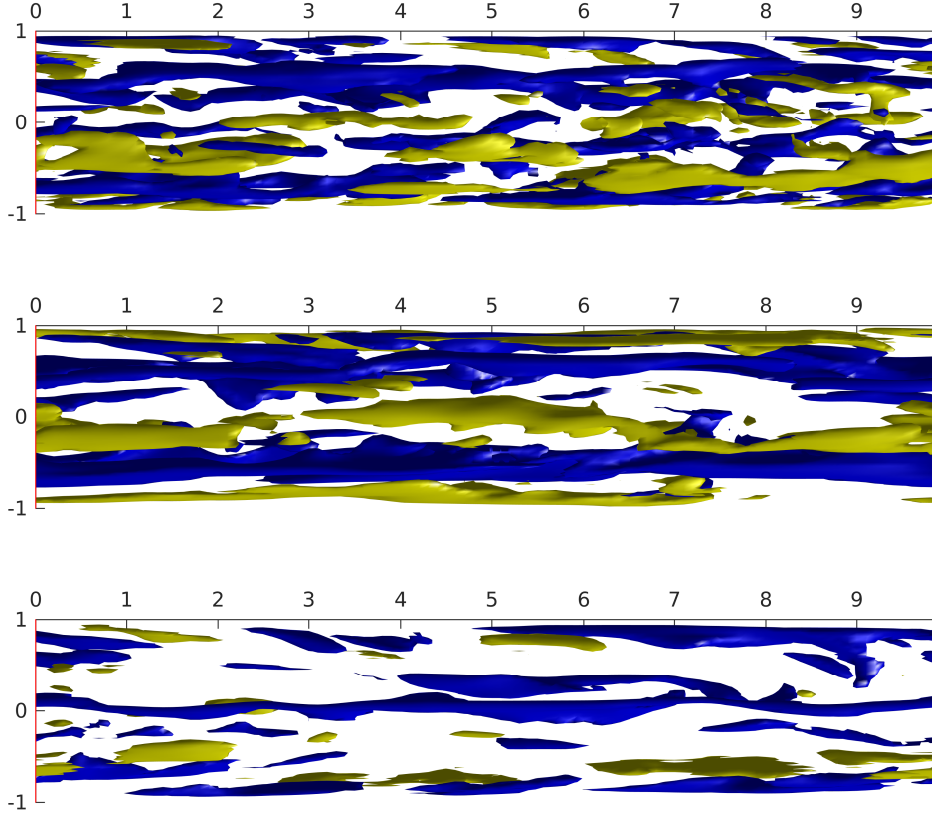


Figure 17: Three-dimensional visualisations of low (blue) and high (yellow) speed streaks in the isothermal (top), heated (middle) and EPG (bottom) flows. Isosurfaces of turbulent streamwise velocity normalised by the corresponding apparent friction velocity $u'_z/u_{\tau p} = \pm 4$.

Comparison between the isothermal and heated flows show that the streaks are relatively unaffected, while vortices are significantly weakened. Our interpretation is that while the streaks are responsible for the saturation of the nonlinearity of the flow, via nonlinear normality of the mean flow (Waleffe 1995), it is relatively ‘easy’ to produce streaks. Note that the mean axial flow for these cases is almost identical (figure 3), and at the end of §3.3 large initial amplifications of disturbances remains possible in the heated case. It is observed that weaker vortices in the heated case are sufficient to produce saturated streaks of the same amplitude. Thus, vortices are more important in the sense that criticality for transition occurs when the vortices are too weak. Comparing now the heated flow with the EPG flow, consistent with the observations of HHS (see their figure 19), it can be seen that the streaks in the latter are weaker than those in the heated flow, but the vortices are of similar strength. Thus relaminarisation is consistent with criticality of the EPG flow.

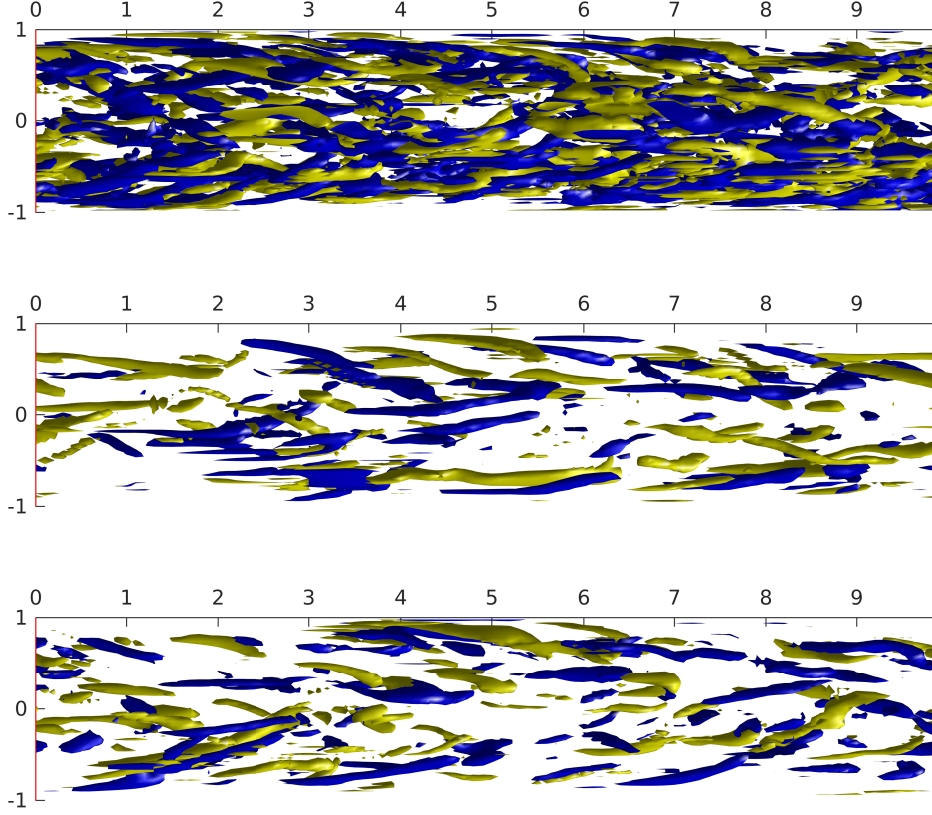


Figure 18: Three dimensional visualisations of vortical structures in the isothermal (top), heated (middle) and EPG (bottom) flows. Isosurfaces of streamwise vorticity fluctuations normalised by the corresponding apparent friction velocity $\omega'_z/u_{\tau p} = \pm 35$.

4. Conclusions

In this paper we have studied the flow of fluid through a vertically-aligned heated pipe using direct numerical simulations (DNS), linear stability and nonlinear travelling-wave solution analyses. The flow is driven by an externally applied pressure gradient and aided by the buoyancy resulting from the lightening of the fluid close to the heated wall. DNS were performed for a range of Reynolds numbers Re and buoyancy parameters C , where the latter measures the magnitude of the buoyancy force relative to the the pressure gradient of the laminar isothermal shear flow, and three different flow regimes were identified – laminar flow, shear-driven turbulence and convection-driven flow – depending on the flow parameters. At relatively low $Re \lesssim 3500$ turbulence is completely suppressed (relaminarised) by buoyancy and as C is increased convection starts driving a relatively quiescent flow. For larger Re , instead, the shear-driven turbulent flow transitions directly to the convection-driven state. Consistent with the appearance of the convective state observed in simulations, a linear instability was found at $C \approx 4$, roughly independent of Re for most of the range considered. The effect of increasing C can be compared to that of increasing polymer concentration, or Weissenberg number, which is known to have a drag reducing effect on turbulent flows (Virk *et al.* 1967). Similarly to our phase diagram

in figure 5, regions of laminar, Newtonian turbulence and elastoinertial turbulence have been identified in this case (Choueiri *et al.* 2018; Lopez *et al.* 2019).

Cases where turbulence is suppressed exhibit a flattened mean streamwise velocity profile. In agreement with recent observations by Kühnen *et al.* (2018) and Marensi *et al.* (2019) on the effect of flattening, we found that states that mediate turbulence (lower-branch travelling wave solutions) are “pushed out” from the laminar state, i.e. as C increases, a larger perturbation amplitude or larger Re are required to drive shear turbulence until, for sufficiently large C , the travelling wave is suppressed altogether.

Finally, we used the relaminarisation criterion recently proposed by He *et al.* (2016), based on an “apparent Reynolds number” of the flow, to predict the critical $C = C_{cr,1}(Re)$ above which the flow will be laminarised or switch to the convection-driven type. This apparent Reynolds number is based on an apparent friction velocity associated with only the pressure force of the flow (i.e. excluding the contribution of the body force/buoyancy). Bistability between shear or convection-driven states was found to occur in the region $4 \lesssim C \lesssim C_{cr,1}$ where the flow may or may not be laminarised depending on the initial flow of the simulation or experiment. Comparison of the turbulent flow structures (rolls and streaks) with those of two reference flows - the flow of equivalent pressure gradient (EPG) and that of equivalent mass flux (EFR) - suggests that near criticality for relaminarisation the vortices, rather than the streaks, are more important in the sense that criticality for transition occurs when the vortices are too weak. This picture is not necessarily inconsistent with Kühnen’s interpretation where relaminarisation is attributed to reduced ability to produce streaks in the presence of the flattened base profile (Kühnen *et al.* 2018). In that purely hydrodynamic setting, the change in the amplitude of streaks and vortices are necessarily coupled. In the heated case, it is possible to differentiate between the role of streaks and vortices.

5. Acknowledgments

This work was funded by EPSRC grant EP/P000959/1.

Appendix A. Link between upward-heated and downward-cooled cases

Consider the axial force from the pressure gradient and buoyancy terms in (2.9). Ignoring the factor $4/Re$ that multiplies all terms, let

$$1 + \beta + C \Theta = 1 + \tilde{\beta} + \tilde{C} \tilde{\Theta}. \quad (\text{A } 1)$$

with $C > 0$ for the upward heated case on the left hand side. Let the right hand side represent the downward cooled case, taking $\tilde{\Theta} = 1 - \Theta$ so that $\tilde{\Theta}$ is coolest on the boundary ($\tilde{\Theta} = 1 - r^2$ for the laminar case). Put $\tilde{C} = -C < 0$, as buoyancy due to positive temperature variations oppose the pressure gradient. (Cooling, however, aids the downward flow.) Substituting in (A 1) we find $\tilde{\beta} = \beta + C$, i.e. the systems differ only by a known offset in the pressure gradient required to maintain volume flux.

Appendix B. Turbulent base flow and eddy viscosity

The turbulent mean flow profile for a pipe may be written $\mathbf{U} = U(y)\hat{\mathbf{z}}$, where $y = 1 - r$ is the dimensionless distance from the boundary wall and r is the radial coordinate.

Applying the Boussinesq eddy viscosity to model for the turbulent Reynolds-stresses, the streamwise component of the Reynolds-averaged momentum conservation reads

$$\frac{1}{Re} \left(\frac{1}{r} + \partial_r \right) (\nu_T \partial_r U) = \partial_z P, \quad (\text{B } 1)$$

where the total effective viscosity is $\nu_T(y) = 1 + \nu_t(y)$ and ν_t is the eddy-viscosity, normalised such that $\nu_T(0) = 1$, i.e. the kinematic value is attained at the wall.

To calculate ν_t it is convenient to use the expression originally suggested for pipe flow by Cess (1958), later used for channel flows by Reynolds & Tiederman (1967) and then by many others (Butler & Farrell 1993; Del Alamo & Jimenez 2006; Pujals *et al.* 2009):

$$\nu_t(y) = \frac{1}{2} \left\{ 1 + \frac{\kappa^2 \hat{R}^2 \hat{B}}{9} (2y - y^2)^2 (3 - 4y + 2y^2)^2 \left[1 - e^{\frac{-y \hat{R} \sqrt{\hat{B}}}{A^+}} \right]^2 \right\}^{\frac{1}{2}} - \frac{1}{2}. \quad (\text{B } 2)$$

Here, $\hat{R} = Re/2$, $\hat{B} = 2B$, with $B = -\partial_z P$ being the averaged streamwise pressure gradient. The parameters $A^+ = 27$ and $\kappa = 0.42$ have been chosen to fit the more recent observations of (McKeon *et al.* 2005).

For the calculation of §3.4, the (apparent) pressure gradient B and (apparent) Re_p are known. The corresponding (EPG) mass flux Reynolds number Re is not yet known, and we wish to determine ν_t . An initial estimate for Re is obtained from from the approximation of Blasius (1913), which may be written

$$Re_p = \frac{0.0791}{16} Re^{1.75}. \quad (\text{B } 3)$$

Then, (B 2) can be used to calculate $\nu_t(r)$, but we must check consistency with (B 1). The latter equation can be inverted for $U(r)$, and, as it has been non-dimensionalised with the same scales of section §2.1, the mean velocity $U_b = 2 \int_0^1 U(r) r dr$ should be 0.5. It will not be exactly so, as the flux-Reynolds number Re has only been estimated. A better estimate is then given by $Re := (0.5/U_b) Re$, so that ν_t can be recalculated and iteratively improved.

REFERENCES

- AVILA, M., MELLIBOVSKY, F., ROLAND, N. & HOF, B. 2013 Streamwise-localized solutions at the onset of turbulence in pipe flow. *Phys. Rev. Lett.* **110**, 224502.
- BAE, Y. Y. 2016 A new formulation of variable turbulent Prandtl number for heat transfer to supercritical fluids. *Intl. J. Heat Mass Transfer* **92**, 792–806.
- BLASIUS, H. 1913 Das Ähnlichkeitsgesetz bei reibungsvorgängen in flüssigkeiten. In *Mitteilungen über Forschungsarbeiten auf dem Gebiete des Ingenieurwesens*, pp. 1–41. Springer.
- BUDANUR, N.B., SHORT, K.Y., FARAZMAND, M., WILLIS, A.P. & CVITANOVIĆ, P. 2017 Relative periodic orbits form the backbone of turbulent pipe flow. *J. Fluid Mech.* **833**, 274–301.
- BUTLER, K. M. & FARRELL, B. F. 1993 Optimal perturbations and streak spacing in wall-bounded turbulent shear flow. *Phys. Fluids A* **5** (3), 774–777.
- CESS, R. D. 1958 A study of the literature on heat transfer in turbulent tube flow. *Tech. Rep.* Tech. Rep. Rep. 8-0529-R24. Westinghouse Research.
- CHOUERI, G. H., LOPEZ, J. M. & HOF, B. 2018 Exceeding the asymptotic limit of polymer drag reduction. *Phys. Rev. Lett.* **120** (12), 124501.
- DEL ALAMO, J. C. & JIMENEZ, J. 2006 Linear energy amplification in turbulent channels. *J. Fluid Mech.* **559**, 205–213.
- DRAZIN, P. & REID, W. H. 2004 *Hydrodynamic Stability*, 2nd edn. Cambridge: Cambridge Univ. Press.
- DUGUET, Y., WILLIS, A. P. & KERSWELL, R. R. 2008 Transition in pipe flow: the saddle structure on the boundary of turbulence. *J. Fluid Mech.* **613**, 255–274.
- ECKHARDT, B., SCHNEIDER, T. M., HOF, B. & WESTERWEEL, J. 2007 Turbulence transition in pipe flow. *Ann. Rev. Fluid Mech.* **29**, 447–468.
- FAISST, H. & ECKHARDT, B. 2003 Traveling waves in pipe flow. *Phys. Rev. Lett.* **91**, 224502.
- HE, S., HE, K. & SEDDIGHI, M. 2016 Laminarisation of flow at low Reynolds number due to streamwise body force. *J. Fluid Mech.* **809**, 31–71.
- HOF, B., VAN DOORNE, C. W. H., WESTERWEEL, J., NIEUWSTADT, F. T. M., FAISST, H., ECKHARDT, B., WEDIN, H., KERSWELL, R. R. & WALEFFE, F. 2004 Experimental observation of nonlinear traveling waves in turbulent pipe flow. *Science* **305**, 1594–1598.
- ITANO, T. & TOH, S. 2001 The dynamics of bursting process in wall turbulence. *J. Phys. Soc. Japan* **70**, 701–714.
- JACKSON, J. D., COTTON, M. A. & AXCELL, B. P. 1989 Studies of mixed convection in vertical tubes. *Intl J Heat Fluid Flow* **10** (1), 2–15.
- KAWAHARA, G., UHLMANN, M. & VAN VEEN, L. 2012 The significance of simple invariant solutions in turbulent flows. *Annu. Rev. Fluid Mech.* **44**, 203–225.
- KERSWELL, R. R. 2005 Recent progress in understanding the transition to turbulence in a pipe. *Nonlinearity* **18**, R17–R44.
- KERSWELL, R. R. 2018 Nonlinear nonmodal stability theory. *Annu. Rev. Fluid Mech.* **50** (1).
- KERSWELL, R. R. & TUTTY, O.R. 2007 Recurrence of travelling waves in transitional pipe flow. *J. Fluid Mech.* **584**, 69–102.
- KIM, W. S., HE, S. & JACKSON, J. D. 2008 Assessment by comparison with dns data of turbulence models used in simulations of mixed convection. *Intl J. Heat Mass Transfer* **51** (5-6), 1293–1312.
- KÜHNEN, J., SONG, B., SCARSELLI, D., BUDANUR, N. B., RIEDL, M., WILLIS, A. P., AVILA, M. & HOF, B. 2018 Destabilizing turbulence in pipe flow. *Nat. Phys.* **14**, 386–390.
- LOPEZ, J. M., CHOUERI, G. H. & HOF, B. 2019 Dynamics of viscoelastic pipe flow at low reynolds numbers in the maximum drag reduction limit. *J. Fluid Mech.* **874**, 699–719.
- MARENSI, E., WILLIS, A. P. & KERSWELL, R. R. 2019 Stabilisation and drag reduction of pipe flows by flattening the base profile. *J. Fluid Mech.* **863**, 850–875.
- MCKEON, B.J., ZAGAROLA, M.V. & SMITS, A.J. 2005 A new friction factor relationship for fully developed pipe flow. *J. Fluid Mech.* **538**, 429–443.
- NAGATA, M. 1990 Three-dimensional finite-amplitude solutions in plane Couette flow: Bifurcation from infinity. *J. Fluid Mech.* **217**, 519–527.
- PRINGLE, C. C. T., DUGUET, Y. & KERSWELL, R. R. 2009 Highly symmetric travelling waves in pipe flow. *Phil. Trans. Royal Soc. A* **367**, 457–472.

- PRINGLE, C. C. T. & KERSWELL, R. R. 2007 Asymmetric, helical, and mirror-symmetric traveling waves in pipe flow. *Phys. Rev. Lett.* **99**, 074502.
- PUJALS, G., GARCÍA-VILLALBA, M., COSSU, C. & DEPARDON, S. 2009 A note on optimal transient growth in turbulent channel flows. *Phys. Fluids* **21** (1), 015109.
- REYNOLDS, W.C. & TIEDERMAN, W.G. 1967 Stability of turbulent channel flow, with application to malkus's theory. *J. Fluid Mech.* **27** (2), 253–272.
- SCHMID, P. J. & HENNINGSON, D. S. 2001 *Stability and Transition on Shear Flows*, , vol. 142. Springer Science & Business Media.
- SCHNEIDER, T. M. & ECKHARDT, B. 2006 Edge of chaos in pipe flow. *Chaos* **16**, 041103.
- SCHNEIDER, T. M., ECKHARDT, B. & YORKE, J. 2007 Turbulence, transition, and the edge of chaos in pipe flow. *Phys. Rev. Lett.* **99**, 034502.
- SENOO, T., DEGUCHI, K. & NAGATA, M. 2012 Bifurcation of internally heated flow in a vertical pipe. *HEFAT 2012* .
- VIRK, P. S., MERRILL, E. W., MICKLEY, H. S., SMITH, K. A. & MOLLO-CHRISTENSEN, E. L. 1967 The Toms phenomenon: turbulent pipe flow of dilute polymer solutions. *J. Fluid Mech.* **30** (2), 305–328.
- VISWANATH, D. 2007 Recurrent motions within plane Couette turbulence. *J. Fluid Mech.* **580**, 339–358, .
- WALEFFE, F. 1995 Transition in shear flows: Nonlinear normality versus non-normal linearity. *Phys. Fluids* **7**, 3060–3066.
- WALEFFE, F. 2001 Exact coherent structures in channel flow. *J. Fluid Mech.* **435**, 93–102.
- WEDIN, H. & KERSWELL, R. R. 2004 Exact coherent structures in pipe flow: Traveling wave solutions. *J. Fluid Mech.* **508**, 333–371.
- WILLIS, A. P. 2017 The Openpipeflow Navier–Stokes solver. *SoftwareX* **6**, 124–127.
- WILLIS, A. P., CVITANOVIĆ, P. & AVILA, M. 2013a Revealing the state space of turbulent pipe flow by symmetry reduction. *J. Fluid Mech.* **721**, 514–540, .
- WILLIS, A. P., CVITANOVIĆ, P. & AVILA, M. 2013b Revealing the state space of turbulent pipe flow by symmetry reduction. *J. Fluid Mech.* **721**, 514–540.
- WILLIS, A. P., HWANG, Y. & COSSU, C. 2010 Optimally amplified large-scale streaks and drag reduction in turbulent pipe flow. *Phys. Rev. E* **82**, 036321.
- WILLIS, A. P., SHORT, K. Y. & CVITANOVIĆ, P. 2016 Symmetry reduction in high dimensions, illustrated in a turbulent pipe. *Phys. Rev. E* **93**, 022204.
- YOO, J. Y. 2013 The turbulent flows of supercritical fluids with heat transfer. *Ann. Rev. Fluid Mechanics* **45**, 495–525.
- YOU, J., YOO, J. Y. & CHOI, H. 2003 Direct numerical simulation of heated vertical air flows in fully developed turbulent mixed convection. *Intl J. Heat Mass Transfer* **46** (9), 1613–1627.